Turbulent Regimes in Collisions of 3D Alfvén-wave Packets

S. Cerri, T. Passot, D. Laveder, P.-L. Sulem, M. Kunz

The Astrophysical Journal, 939:36 (13pp), 2022 November 1 https://doi.org/10.3847/1538-4357/ac93fe

Turbulent Regimes in Collisions of 3D Alfvén-wave Packets

S. S. Cerri[1], T. Passot[1], D. Laveder[1], P.-L. Sulem[1], and M. W. Kunz[2,3]
[1] Université Côte d'Azur, Observatoire de la Côte d'Azur, CNRS, Laboratoire Lagrange, Bd de l'Observatoire, CS 34229, 06304 Nice cedex 4, France
silvio.cerri@oca.eu
[2] Department of Astrophysical Sciences, Princeton University, 4 Ivy Lane, Princeton, NJ 08544, USA
[3] Princeton Plasma Physics Laboratory, PO Box 451, Princeton, NJ 08543, USA
Received 2022 July 9; revised 2022 September 16; accepted 2022 September 20; published 2022 November 1

Abstract

Using three-dimensional gyrofluid simulations, we revisit the problem of Alfvén-wave (AW) collisions as building blocks of the Alfvénic turbulent cascade and their interplay with magnetic reconnection at magnetohydrodynamic (MHD) scales. Depending on the large-scale value of the nonlinearity parameter χ_0 (the ratio between the AW linear propagation time and nonlinear turnover time), different regimes are observed. For strong nonlinearities ($\chi_0 \sim 1$), turbulence is consistent with a dynamically aligned, critically balanced cascade—fluctuations exhibit a scale-dependent alignment $\sin\theta_{k_\perp} \propto k_\perp^{-1/4}$, resulting in a $k_\perp^{-3/2}$ spectrum and $k_\parallel \propto k_\perp^{1/2}$ spectral anisotropy. At weaker nonlinearities (small χ_0), a spectral break marking the transition between a large-scale weak regime and a small-scale $k_\perp^{-11/5}$ tearing-mediated range emerges, implying that dynamic alignment occurs also for weak nonlinearities. At $\chi_0 < 1$ the alignment angle $\theta_{k_\perp}$ shows a stronger scale dependence than in the $\chi_0 \sim 1$ regime, namely $\sin\theta_{k_\perp} \propto k_\perp^{-1/2}$ at $\chi_0 \sim 0.5$, and $\sin\theta_{k_\perp} \propto k_\perp^{-1}$ at $\chi_0 \sim 0.1$. Dynamic alignment in the weak regime also modifies the large-scale spectrum, scaling approximately as $k_\perp^{-3/2}$ for $\chi_0 \sim 0.5$ and as $k_\perp^{-1}$ for $\chi_0 \sim 0.1$. A phenomenological theory of dynamically aligned turbulence at weak nonlinearities that can explain these spectra and the transition to the tearing-mediated regime is provided; at small χ_0, the strong scale dependence of the alignment angle combines with the increased lifetime of turbulent eddies to allow tearing to onset and mediate the cascade at scales that can be larger than those predicted for a critically balanced cascade by several orders of magnitude. Such a transition to tearing-mediated turbulence may even supplant the usual weak-to-strong transition.

Unified Astronomy Thesaurus concepts: Plasma astrophysics (1261); Space plasmas (1544); Interplanetary turbulence (830); Alfven waves (23); Magnetohydrodynamical simulations (1966); Magnetohydrodynamics (1964); Plasma physics (208)

1. Introduction

A wide range of space and astrophysical systems host turbulent plasmas (e.g., Quataert & Gruzinov 1999; Schekochihin & Cowley 2006; Bruno & Carbone 2013). The turbulent cascade transfers energy from the injection scales down to dissipation scales, where it is converted into heat and nonthermal particles, thus regulating the energetics and/or dynamics of a system. In the last decades, the properties of cascading fluctuations in weakly collisional plasmas have been explored in unprecedented detail, thanks to in situ measurements from spacecraft missions in the solar wind (e.g., Goldstein et al. 1995; Alexandrova et al. 2009, 2021; Podesta et al. 2009; Sahraoui et al. 2010, 2020; Wicks et al. 2010, 2013; Chen 2016; Bruno & Carbone 2013; Chen et al. 2020; Kasper et al. 2021).

At large ("fluid") scales, the cascade may be described as MHD turbulence, with the building blocks of its Alfvénic component being interactions between counterpropagating Alfvén waves (e.g., Iroshnikov 1963; Kraichnan 1965; Goldreich & Sridhar 1995; Howes & Nielson 2013; Oughton & Matthaeus 2020). This Alfvénic cascade is naturally anisotropic with respect to the mean-magnetic-field direction, with field-parallel wavenumbers much less than their field-perpendicular counterparts, $k_\parallel \ll k_\perp$. Assuming a critical balance (CB) between the fluctuations' linear and nonlinear timescales, this cascade was originally predicted by Goldreich & Sridhar (1995) to exhibit a perpendicular spectrum $\propto k_\perp^{-5/3}$ and a spectral anisotropy $k_\parallel \propto k_\perp^{2/3}$, to which corresponds a parallel spectrum $\propto k_\parallel^{-2}$. Still, within the CB assumption, the continuous shearing of fluctuations in the field-perpendicular plane associated with interactions between counterpropagating AW packets was later taken into account by Boldyrev (2006), postulating that fluctuations would be subject to a scale-dependent "dynamic alignment" (or antialignment) whose angle θ_k is such that $\sin\theta_k \propto k_\perp^{-1/4}$. This effect results in a 3D anisotropy of the turbulent fluctuations and a cascade whose spectrum follows $k_\perp^{-3/2}$, with a $k_\parallel \propto k_\perp^{1/2}$ spectral anisotropy (the $k_\parallel^{-2}$ spectrum being unaltered; in this case, $k_\perp$ is related to the shortest length scale λ of these 3D-anisotropic eddies, which is perpendicular to both the mean-field and magnetic-fluctuation direction; see Section 4).

Another fundamental aspect of plasma turbulence is the formation of current sheets (CSs), either as a result of large-scale, broadband injection (e.g., Politano et al. 1995; Biskamp & Müller 2000; Zhdankin et al. 2013; Sisti et al. 2021) or of direct AW-packet interactions (e.g., Pezzi et al. 2017; Verniero et al. 2018; Ripperda et al. 2021). If sufficiently thin and long lived, these CSs can be disrupted by tearing and/or magnetic reconnection (e.g., Carbone et al. 1990; Servidio et al. 2011; Zhdankin et al. 2015; Agudelo Rueda et al. 2021; Ripperda et al. 2021), processes that have been suggested to mediate the nonlinear energy transfer at both MHD (e.g., Carbone et al. 1990; Boldyrev & Loureiro 2017; Mallet et al. 2017b; Comisso et al. 2018; Dong et al. 2018; Tenerani & Velli 2020) and

kinetic (e.g., Cerri & Califano 2017; Franci et al. 2017; Loureiro & Boldyrev 2017; Mallet et al. 2017a) scales. When this disruption occurs, we refer to the resulting turbulence as a "tearing-mediated" cascade, whose range at resistive-MHD scales is characterized by a steep $k_\perp^{-11/5}$ spectrum. The conditions under which a critically balanced, dynamically aligned cascade can mutate into a tearing-mediated cascade at a transition scale $\lambda_* \sim (k_\perp^*)^{-1}$ rely on two criteria: (i) that turbulent eddies are sheared in the field-perpendicular direction to set up a tearing-unstable configuration, and (ii) that these eddies live long enough to allow the tearing instability to grow and disrupt them. While the latter condition depends upon the material properties of the plasma (e.g., the resistivity η), the former is a consequence of the dynamic alignment of turbulent fluctuations that produces eddy anisotropy in the field-perpendicular plane. In this context, regardless of whether dynamic alignment would have proceeded indefinitely until dissipation scales (Perez et al. 2012) or would have been only a limited-range effect tied to the dynamics occurring at the outer scale (Beresnyak 2012), what matters is that alignment occurs on enough scales to meet the condition for tearing instability to grow sufficiently fast (after which alignment will anyway be—partially or completely—disrupted by reconnection events; see Section 3.1.3).

In the fluid regime, the coexistence of a turbulent MHD inertial range with a steeper tearing-mediated regime at smaller (but still, fluid) scales has been evidenced within two-dimensional (2D) simulations (Dong et al. 2018). In 3D, MHD simulations of the plasmoid instability in an inhomogeneous reconnection layer, leading to a self-sustained turbulent state, have, however, only reproduced the "small-scale regime" (Huang & Bhattacharjee 2016). A still-debated point concerns the existence of a tearing-mediated regime in 3D, where there are steep resolution requirements to separate clearly a so-called "disruption scale" (at which a tearing-mediated cascade would begin) from the actual dissipation scale when broadband fluctuations are injected into the system. Here, we approach this problem by investigating interactions between counterpropagating AW packets. In this context, reduced models such as the two-field gyrofluid (2fGF) model (Passot et al. 2018; Passot & Sulem 2019; Miloshevich et al. 2021; Passot et al. 2022) can be extremely useful for isolating and modeling purely Alfvénic turbulence, without being affected by other modes and/or a plethora of kinetic effects (e.g., Howes et al. 2011; Told et al. 2015; Matthaeus et al. 2016; Cerri et al. 2017, 2018, 2021; Grošelj et al. 2017; Perrone et al. 2018; Arzamasskiy et al. 2019; González et al. 2019; Squire et al. 2022).

In this work, we provide the first evidence of a tearing-mediated cascade occurring at MHD scales due to the interaction of counterpropagating 3D AW packets. For weak initial nonlinearities, $\chi_0 < 1$, dynamic alignment of the relatively long-lived fluctuations leads to a strong, tearing-mediated cascade that replaces the more customary weak-to-strong turbulence transition. At $\chi_0 \sim 1$, a dynamically aligned, strong MHD turbulent regime is established instead; a tearing-mediated cascade may eventually emerge, but not at the Lundquist numbers we are able to explore numerically. New scalings for weak turbulence subject to dynamic alignment and for the relevant transition scales are also provided.

2. Two-field Gyrofluid Simulations

2.1. Model Equations

To investigate nonlinear interactions between AW packets and the resulting multiscale turbulent cascade, we employ the two-field gyro-fluid (2fGF) model (Passot et al. 2018), in which small-amplitude, low-frequency fluctuations are taken to be spatially anisotropic with respect to a mean magnetic field (viz., $k_\perp \gg k_\parallel$, where $k_\perp$ and $k_\parallel$ are the wavenumbers perpendicular and parallel to the mean field, respectively). Although this model in general includes the finite inertia of the electrons, here we consider scales such that $k_\perp d_e \ll 1$, where d_e is the electron skin depth. Finite electron-inertia effects can then be ignored and the equations for the number density of electron gyrocenters, N_e, and the field-parallel component of magnetic potential, $A_\parallel$, read

$$\frac{\partial N_e}{\partial t} + [\varphi, N_e] - [B_z, N_e] + \frac{2}{\beta_e}\nabla_\parallel \Delta_\perp A_\parallel = 0, \quad (1)$$

$$\frac{\partial A_\parallel}{\partial t} + \nabla_\parallel(\varphi - N_e - B_z) = 0, \quad (2)$$

where the Poisson bracket of two fields F and G is defined as $[F, G] \doteq (\partial_x F)(\partial_y G) - (\partial_y F)(\partial_x G)$, $\Delta_\perp \doteq \partial_{xx} + \partial_{yy}$ is the Laplacian operator acting perpendicular to $\boldsymbol{B}_0 \doteq B_0 \boldsymbol{e}_z$, and the electrostatic potential φ and parallel magnetic-field fluctuations B_z are related by $B_z = M_1\varphi$ and $N_e = -M_2\varphi$. The operators M_1 and M_2 are represented in Fourier space by $\widehat{M}_1 \doteq L_1^{-1}L_2$ and $\widehat{M}_2 \doteq L_3 + L_4 L_1^{-1} L_2$, where $L_1 \doteq 2/\beta_e + (1+2\tau)(\Gamma_0 - \Gamma_1)$, $L_2 \doteq 1 + (1-\Gamma_0)/\tau - \Gamma_0 + \Gamma_1$, $L_3 \doteq (1-\Gamma_0)/\tau$, and $L_4 \doteq 1 - \Gamma_0 + \Gamma_1$. Here, $\beta_e = 8\pi n_0 T_{e0}/B_0^2$ is the electron plasma beta, $\tau = T_{i0}/T_{e0}$ is the ion-to-electron temperature ratio (so $\beta_i = \tau\beta_e$), and $\Gamma_n(b) \doteq \mathrm{I}_n(b)\exp(-b)$, with I_n being the first-type modified Bessel function of order n and argument $b \doteq k_\perp^2\rho_i^2/2$ ($\rho_i \doteq v_{th,i}/\Omega_{i0}$ is the ion gyroradius and $v_{th,i} \doteq \sqrt{2T_{i0}/m_i}$ the ion thermal speed). Equations (1) and (2) are normalized in terms of the ion-cyclotron frequency $\Omega_{i0} \doteq eB_0/m_i c$ and the ion-sound gyroradius $\rho_s \doteq c_s/\Omega_{i0}$, where $c_s \doteq \sqrt{T_{e0}/m_i}$ is the ion-sound speed.

The 2fGF model effectively reproduces the so-called reduced magnetohydrodynamics (RMHD), or Hall reduced magnetohydrodynamics (HRMHD) if $\tau \ll 1$, when employed at perpendicular scales much larger than the ion gyroradius, $k_\perp\rho_i \ll 1$ (see Passot & Sulem 2019 for various limits of the 2fGF model). Our choice to employ the 2fGF model at MHD scales is motivated by the fact that it allows us to extend our investigations self-consistently to include interactions between Alfvénic wave packets at and below ion scales, which is the subject of a forthcoming paper. The exact linear eigenmodes of the 2fGF system are given by the generalized Elsässer potentials, $\mu^\pm \doteq \Lambda\varphi \pm \sqrt{2/\beta_e}\, A_\parallel$, where $\Lambda \doteq (-\Delta_\perp)^{-1/2}(1 + M_2 - M_1)^{1/2} M_2^{1/2}$. The associated generalized Elsässer fields are $\boldsymbol{z}^\mp = \boldsymbol{e}_z \times \boldsymbol{\nabla}\mu^\pm$; they reduce to the usual Elsässer (1950) fields in the MHD limit.

2.2. Simulation Setup

Equations (1) and (2) are discretized and solved on a 672^3 grid for a $\beta_e = \beta_i = 1$ plasma in a periodic cubic box of length $L_0 = 2\pi\rho_s \times \tilde{\ell}_0$ with $\tilde{\ell}_0 = 336$.[4] A combination of second-order Laplacian dissipation (with resistivity η) and eighth-order

[4] The numerical implementation of the 2fGF model adopts "contracted variables", i.e., quantities along the mean-field direction are rescaled according to a gyrofluid ordering parameter $\epsilon \ll 1$. For example, $L_z^{(code)} = \epsilon L_z^{(real)}$ and $k_z^{(code)} = \epsilon^{-1} k_z^{(real)}$. We have verified that an explicit choice of ϵ does not affect the following analysis.

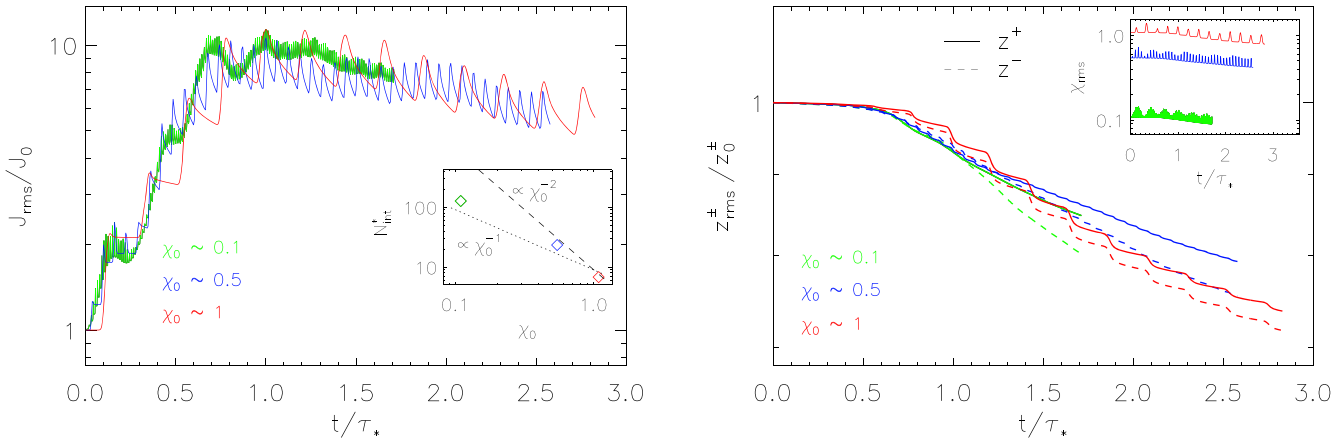

Figure 1. Left: time evolution of the root-mean-square (rms) current density, $J_{\rm rms}$ (normalized to $J_0 = J_{\rm rms}(t=0)$; time is normalized to the time of peak activity τ_*). The inset reports the (measured) number of collisions $N^*_{\rm int} = \tau_*/\tau_{\rm int} = 3\tau_*/\tau_{\rm A}$ required to reach the peak of turbulent activity as a function of the initial nonlinearity parameter χ_0, showing that a fully developed turbulent state is achieved on a timescale shorter than the one associated with the usual weak scaling (using the estimate $\tau_* \sim 3\tau_{\rm nl}$, dotted line is $9/\chi_0$; a dashed line $9/\chi_0^2$ based on the estimate $\tau_* \sim 3\tau_{\rm casc}$ is also given for reference). Right: time evolution of the rms Elsässer fields, $z^{\pm}_{\rm rms}$ (normalized to $z^{\pm}_0 = z^{\pm}_{\rm rms}(t=0)$). The inset shows the time evolution of the rms nonlinearity parameter $\chi_{\rm rms}$.

hyperdissipation operators removes energy close to the grid scale. Our choice of this operator combination and of their coefficients is such that (i) the dissipation scale is always above the ion scales, $k_{\rm diss}\rho_{\rm i} \lesssim 1$, so that the inertial range of the cascade lies in the RMHD regime, and (ii) reconnection, at least at small values of $\chi_0 < 1$, is driven by the Laplacian resistivity η, i.e., there is enough range for a corresponding tearing-mediated cascade before achieving complete energy dissipation within the resolution thanks to the hyperresistivity.[5] Nevertheless, we anticipate some differences at $\chi_0 \sim 1$ versus $\chi_0 < 1$, especially in that we do not expect to resolve k_* (as predicted by Loureiro & Boldyrev 2017 and Mallet et al. 2017b) when $\chi_0 \sim 1$.

Two counterpropagating AW packets are initialized from the following potentials:

$$\mu^{\pm} = \mu^{\pm}_0 \frac{\sin(\boldsymbol{k}^{\pm}_0 \cdot \boldsymbol{x} + \psi^{\pm})}{|\boldsymbol{k}^{\pm}_{\perp,0}|} \exp\left[-\frac{1}{2}\left(\frac{z-\zeta^{\pm}_0}{\sigma^{\pm}_z}\right)^2\right], \quad (3)$$

where $\mu^{\pm}_0$ and $\boldsymbol{k}^{\pm}_0 = k^{\pm}_{z,0}\boldsymbol{e}_z + \boldsymbol{k}^{\pm}_{\perp,0}$ are the initial amplitude and wavevector of the packets (centered at $z = \zeta^{\pm}_0$ with standard deviation $\sigma^{\pm}_z$), and $\psi^{\pm}$ is a random phase. The packets' initial positions and widths are $\zeta^{+}_0 = L_0/4$, $\zeta^{-}_0 = 3L_0/4$, and $\sigma^{\pm}_z = \tilde{\ell}_0/3$. All simulations have the same initial amount of energy in the two Elsässer fields, viz. $\int|\boldsymbol{z}^+|^2 \, {\rm d}\boldsymbol{x} = \int|\boldsymbol{z}^-|^2 \, {\rm d}\boldsymbol{x}$, which is initially carried by modes $\boldsymbol{k}^{+}_0 L_0/2\pi = (1, 0, 1)$ and $\boldsymbol{k}^{-}_0 L_0/2\pi = (0, 1, -2)$. The slight asymmetry in $k^{\pm}_{z,0}$ causes a minor imbalance during the subsequent evolution (of order $\lesssim 5\%$; Figure 1, right panel). This is consistent with the von Karman–Howarth decay law (e.g., Wan et al. 2012 and references therein), i.e., ${\rm d}(z^{\pm})^2/{\rm d}t \propto -(z^{\mp}/\lambda_{\pm})(z^{\pm})^2$, with the similarity length estimated as $\lambda_{\pm} \sim 1/k^{\pm}_0$ (implying a slightly faster decay of z^- in our setup).

Three different regimes defined by the initial nonlinearity parameter of the AW packets are considered: $\chi_0 \sim 0.1$, ~ 0.5, and ~ 1, where $\chi_0 = \tau_{\rm lin}/\tau_{\rm nl} \approx (k_{\perp,0}\delta B_{\perp,0})/(k_{z,0}B_0)$ (e.g., see Miloshevich et al. 2021). The associated Lundquist numbers defined using the (second-order) resistivity $S_0 = L_0 v_{\rm A}/\eta$ are $\approx 1.7\times10^6$, $\approx 3.3\times10^5$, and $\approx 1.7\times10^5$, respectively; these correspond to the same magnetic Reynolds number $R_{\rm m} \doteq L_0 u_{\rm rms}/\eta \approx 2.2\times10^5$ for all simulations. Note that achieving these values for the Lundquist and magnetic Reynolds numbers associated to the Laplacian resistivity has been only possible by simultaneously employing an eighth-order hyperdissipation operator (whose coefficient has been carefully chosen following a detailed convergence study).

2.3. Timescales of the Problem

There are three important timescales that govern the dynamics of the cascade. The first is the interaction time defined by $\tau^{-1}_{\rm int} = (\tau^{+}_{\rm lin})^{-1} + (\tau^{-}_{\rm lin})^{-1} = (2\pi)^{-1}(k^{+}_{\parallel}v_{\rm A} + k^{-}_{\parallel}v_{\rm A})$, the time between two consecutive collisions of AW packets. In our setup, $\tau_{\rm int} = \tau_{\rm A}/3$, where $\tau_{\rm A} \doteq L_0/v_{\rm A}$ is the Alfvén crossing time. The second timescale is τ_*, the time at which the turbulence reaches its "peak activity", estimated as a multiple N_* of the nonlinear timescale $\tau_{\rm nl} \approx \tau_{\rm A}/\chi_0$. Note that smaller values of χ_0 correspond to larger $\tau_{\rm nl}$. Usually, a few nonlinear times are required to reach a peak in the rms current density, $J_{\rm rms}$ (e.g., Servidio et al. 2011); we find $N_* \approx 3$ in our simulations. Fully developed turbulence should thus be reached after $N^*_{\rm int} = \tau_*/\tau_{\rm int} \sim 9/\chi_0$ collisions (Figure 1, left-panel inset, dotted line). This number is noticeably smaller than implied by standard weak-turbulence estimates,[6] for which τ_* would be a few cascade times; e.g., by analogy, if $\tau_* \sim 3\tau_{\rm casc} \approx 3\tau_{\rm nl}/\chi_0$, then $N^* \sim 9/\chi_0^2$ (inset, dashed line). The difference between the data and the weak-turbulence estimate motivates the introduction of a third timescale, the inverse growth rate of the tearing instability, $(\gamma^{\rm t})^{-1}$. If $\gamma^{\rm t}_{k_*}\tau_{{\rm nl},k_*} \gtrsim 1$ at some scale k_*,

[5] This has been verified by running more than 50 simulations on a 560^3 grid (keeping the resolution fixed by reducing $\tilde{\ell}_0$) testing different combinations of dissipation operators and finding their optimal coefficients. See the Appendix for a summary of these numerical tests.

[6] Even at $\chi_0 \ll 1$, our setup may not necessarily satisfy some working assumptions that are typical of standard weak-turbulence (WT) theory. WT theory assumes (weak) interactions between a sea of different, randomly phased waves, whereas in our simulations, the (weak) interactions always occur between the same two (randomly phased) waves. Although the simulated turbulence is weak at large scales when $\chi_0 < 1$, this somewhat artificial setup may invalidate the "random-walk argument" leading to the $N* \propto \chi^{-2}$ scaling in standard WT theory.

the tearing instability is able to feed off of the associated current sheet in the cascade before the host eddy decorrelates through nonlinear interactions. Such a transition scale in the strong $\chi_0 \sim 1$ regime of MHD turbulence has been shown to scale as $k_* L_0 \propto S_0^{4/7}$ by a number of authors (e.g., Loureiro & Boldyrev 2017; Mallet et al. 2017b; Comisso et al. 2018). Because $\tau_{\rm nl}$ is larger for smaller χ_0, this tearing condition should be easier to satisfy at larger scales (smaller k_*) for weak nonlinearities than in strong turbulence. The idea that a tearing-mediated range could emerge within a weakly nonlinear cascade also relies implicitly on the fact that, analogously to what was postulated by Boldyrev (2006) for strong turbulence, some sort of dynamic alignment of turbulent fluctuations occurs in the weak regime as well so that the fluctuations become 3D anisotropic. In Section 3.1.3 we show that this is indeed the case and that the observed scalings (which differ significantly from those predicted for strong turbulence by Boldyrev 2006) can be explained by a phenomenological theory for dynamically aligned weak turbulence (Section 4.1). This argument is one motivation for our focus on $\chi_0 < 1$, since it implies that less numerical resolution is required to realize tearing-mediated turbulence at small χ_0 than within a dynamically aligned, critically balanced state having $\chi_0 \sim 1$ (Section 4.2). We will additionally argue that CB is induced by reconnection in the tearing-mediated range, and that this may explain both the observed fluctuations' scaling in this range and the reduced number of AW-packet interactions, $N_{\rm int}^* \propto \chi_0^{-1}$ instead of $N_{\rm int}^* \propto \chi_0^{-2}$, needed to achieve the peak activity at low χ_0 (Section 4.3).

3. Numerical Results

Simulations are performed for a few τ_* (Figure 1), corresponding to a large number of AW-packet collisions (e.g., $N_{\rm int}^{(\rm tot)} \approx 200$ at $\chi_0 \sim 0.1$). If not stated otherwise, the fluctuations' properties are determined by averaging over a time interval $\Delta t \approx 0.8\tau_*$ around peak activity.

3.1. Fluctuations' Properties at Peak Activity

As AW packets shear one another in the plane perpendicular to $\boldsymbol{B}_0$, they generate strong CSs (evidenced by the short-time oscillations in $J_{\rm rms}$; Figure 1). Each interaction increases the magnetic shear in the CSs, thus increasing $J_{\rm rms}$ until "peak activity" is eventually achieved.

3.1.1. Current-sheet Disruption and Structure of AW Packets

Figure 2 shows perpendicular magnetic-field fluctuations, $\delta B_\perp / B_{\rm rms}$, both in the x–z plane (left column) and in the x–y plane (right column) at $t/\tau_* \simeq 1.35$, after turbulence has developed. At this time, AW packets are still clearly distinguishable in the x–z plane (left column), with more fine-scale structure visible within the packets with increasing χ_0 (top to bottom). These are related to CS structures formed through AW-packet collisions (e.g., Pezzi et al. 2017; Verniero et al. 2018), which are then affected by the tearing instability occurring within them. At $\chi_0 \sim 0.1$, they are well localized in x and have essentially no structure along z (Figure 2, top-left panel). The occurrence of finer structures along z (corresponding to the generation of small-$k_\parallel$ scales; see Section 3.1.2) increases with increasing χ_0 (Figure 2, middle-left and bottom-left panels, respectively). While the bulk of the AW packets are still distinguishable in all regimes, the structure of $\delta B_\perp$ in the plane perpendicular to $\boldsymbol{B}_0$ exhibits clear differences. The "relics" of disrupted CSs are especially recognizable at $\chi_0 \sim 0.1$, where $\delta B_\perp$ fluctuations indeed resemble small-scale, plasmoid-like structures in 2D (i.e., quasi-circular magnetic structures referred to as "magnetic islands" in 2D, which in 3D actually manifest as flux ropes; Figure 2, top-right panel). At $\chi_0 \sim 0.5$, such structures are also visible, although $\delta B_\perp$ fluctuations are now less organized into plasmoid-like structures within the disrupted CSs (this difference reflects on the low-$k_\perp$ part of the $\delta B_\perp$ energy spectrum; see Section 3.1.2). $\delta B_\perp$ fluctuations are clearly different at $\chi_0 \sim 1$, where no large-scale CS structures are distinguishable in the perpendicular plane (Figure 2, bottom-right panel): This is qualitatively similar to 3D turbulence arising from broadband injection (see, e.g., Figure 1 of Cerri et al. 2019).

3.1.2. Fluctuations' Spectrum and Anisotropy

As a result of AW interaction and CS disruption, a cascade of $\delta B_\perp$ fluctuations develops (Figure 3). At $\chi_0 \sim 0.1$ and ~ 0.5 (green and blue curves, respectively), the $\delta B_\perp$ energy spectra exhibit a break at $k_\perp \rho_{\rm i} \approx 0.05$ (Figure 3, top-left panel), which we identify as the transition scale k_*. Both simulations indeed show a "small-scale" MHD spectrum below k_* proportional to $k_\perp^{-\alpha}$ with spectral index $2.1 \lesssim \alpha \lesssim 2.3$ (Figure 3, bottom-left panel), consistent with predictions for tearing-mediated turbulence (viz. between $k_\perp^{-11/5}$ and $k_\perp^{-19/9}$; see, e.g., Mallet et al. 2017b; Boldyrev & Loureiro 2017; Comisso et al. 2018; Tenerani & Velli 2020). Such a spectral break is instead not present in the $\chi_0 \sim 1$ case, consistent with the expectation that strong turbulence would require a larger S_0 to resolve k_* (see Section 4.2). At $k_\perp \rho_{\rm i} \lesssim 0.05$, however, the two regimes develop a different power law (although of limited extent), close to $-3/2$ at $\chi_0 \sim 0.5$ and to -1 at $\chi_0 \sim 0.1$. Although it would be appealing to interpret the $-3/2$ spectrum within the context of a dynamically aligned, strong MHD turbulent cascade (Boldyrev 2006; Chandran et al. 2015; Mallet & Schekochihin 2017), we found $\chi_k < 1$ at $k_\perp < k_*$ (not shown). Analogously, the -1 spectrum may be due to a not-yet-developed large-scale turbulent state, or perhaps to nonlocal transfer between the AW packets and the disruption scale through CS structures (cf. Figure 4 in Franci et al. 2017). Nevertheless, fluctuations at both $\chi_0 \sim 0.1$ and ~ 0.5 show a spectral anisotropy $k_\parallel / k_\perp$ consistent with the weak-turbulence regime at $k_\perp < k_*$ (i.e., $k_\parallel \approx$ const; Figure 3, right panel). A possible alternative explanation for the above spectra in terms of dynamic alignment in weak turbulence is provided in Section 4. On the other hand, the formation of a $k_\perp^{-3/2}$ spectrum at $\chi_0 \sim 1$ (Figure 3, left panels, red curve) is consistent with dynamic alignment in strong MHD turbulence. This seems to be confirmed by the measured spectral anisotropy $k_\parallel \propto k_\perp^{1/2}$ (Figure 3, right panel).

3.1.3. Fluctuations' Alignment Angle

As anticipated in Section 2.3, the possibility of activating a tearing-mediated cascade relies not only on the fact that turbulent eddies are sheared in the field-perpendicular direction to set up a tearing-unstable configuration but also on the requirement that these eddies live long enough to allow tearing instability to grow and disrupt them. The former is a consequence of the dynamic alignment of turbulent fluctuations in that plane, which ultimately gives the fluctuations a 3D

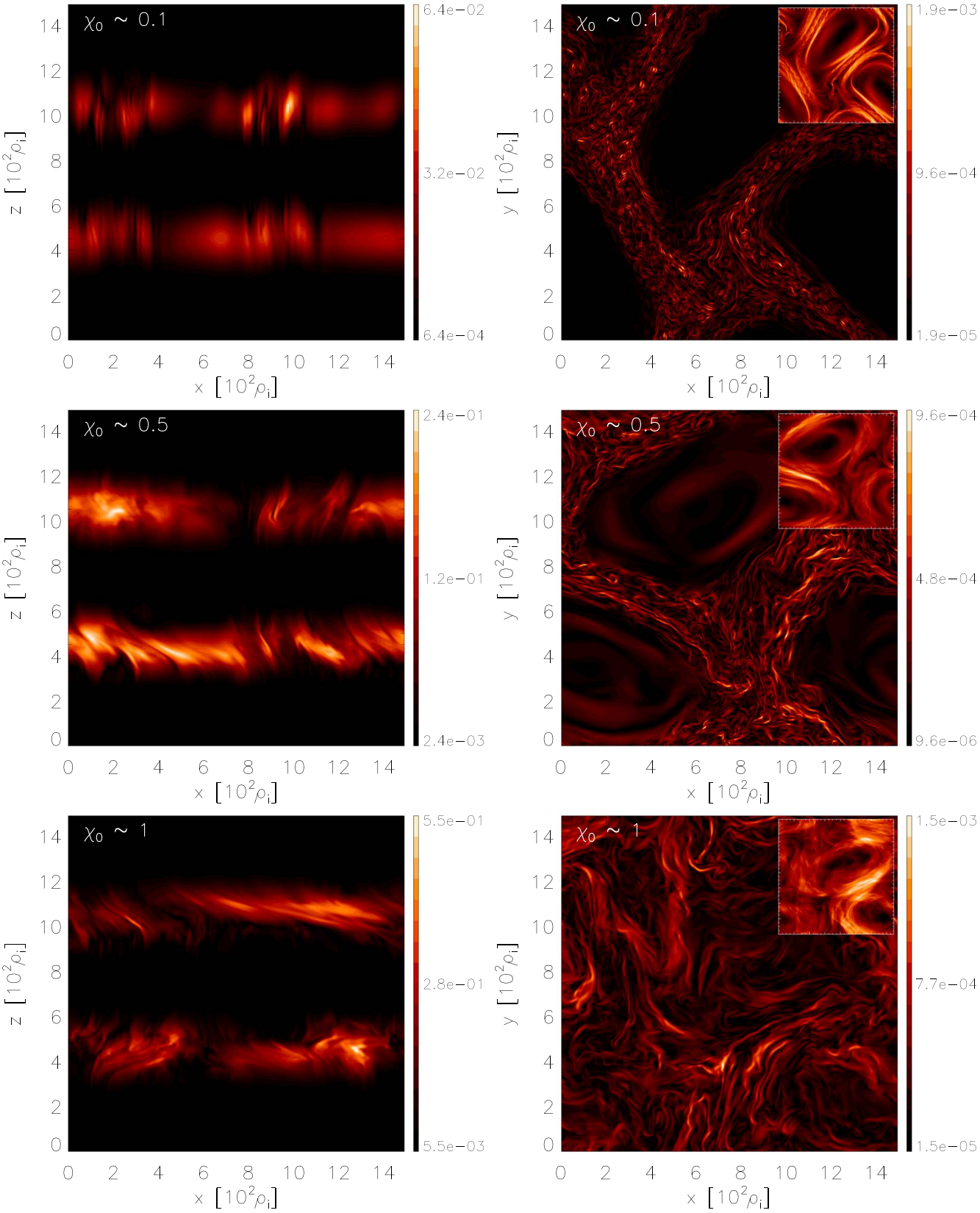

Figure 2. Isocontours of $\delta B_\perp/B_{\rm rms}$ in the x–z plane at $y = L_0/2$ (left column) and in the x–y plane at $z = L_0/2$ (right column), at $t/\tau_* \simeq 1.35$ (in the developed turbulent regime) for initial nonlinearity parameter $\chi_0 \sim 0.1$, ~ 0.5, and ~ 1 (from top to bottom). Recall that $\boldsymbol{B}_0$ is along z. Insets: isocontours of $\delta B_\perp/B_{\rm rms}$ averaged over z (see lagrange.oca.eu/fr/silvio-cerri/3794-animations for animations).

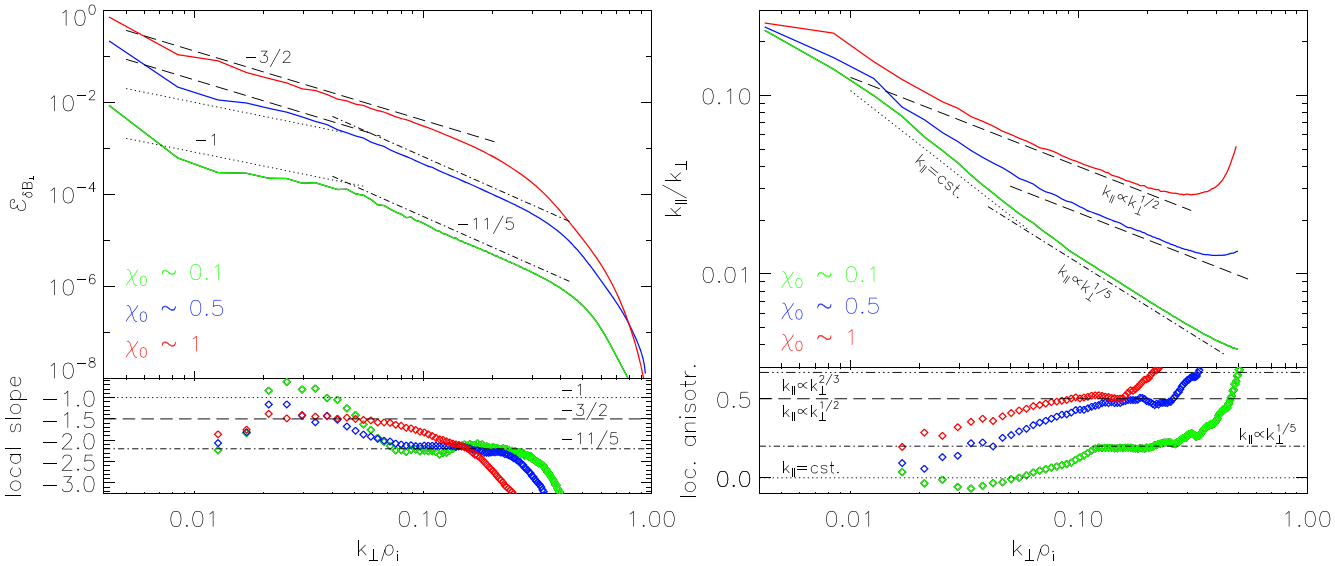

Figure 3. Left: $\delta B_\perp$ energy spectrum and its local slope vs. $k_\perp \rho_i$. Spectra are time-averaged over $0.9 \lesssim t/\tau_* \lesssim 1.7$. Right: spectral anisotropy $k_\parallel/k_\perp$ averaged over the same time interval ($k_\parallel(k_\perp)$ is obtained using the method presented in Cho et al. (2002)). Relevant power laws are provided for reference.

spectral anisotropy. However, once reconnection sets in, the effect of the eddies' disruption by the tearing instability is to interrupt the achieved cascade-induced alignment by producing plasmoid-like structures (i.e., replacing the elongated sheet-like structure of the eddy in the field-perpendicular plane with quasi-circular magnetic islands—flux ropes, in 3D); this process instead *increases* the alignment angle (i.e., produces "misalignment"; see, e.g., Mallet et al. 2017b; Boldyrev & Loureiro 2017; Comisso et al. 2018). This is interpreted by Mallet et al. (2017b) in terms of a discrete and recursive view of the cascade: Once the cascade enters the tearing-mediated range $\lambda \lesssim \lambda_*$, there will be a "reset" of the fluctuations' alignment angle and amplitude due to the eddy disruption—increasing the former and decreasing the latter—followed by a range in which these fluctuations cascade further toward smaller scales while re-aligning until the condition for tearing-induced disruption is achieved, again "resetting" the alignment and amplitude, and so on until dissipation sets in (see discussion in their Section 6). On the other hand, Boldyrev & Loureiro (2017) and Comisso et al. (2018) assume that, below λ_*, the fluctuations will keep misaligning with decreasing scale, with the scaling $\sin\theta_\lambda \propto \lambda^{-4/5}$. This scaling is based solely on the physics of tearing instability, i.e., on the scalings of the nonlinear Coppi mode (Coppi et al. 1976) and thus formally belongs to a pure tearing-mediated cascade (i.e., occurring homogeneously in space and time). The recursive-disruption view of Mallet et al. (2017b) also produces a scale-dependent alignment angle, which is constrained within an envelope whose boundary scales as $\lambda^{-4/5}$ (see Section 7.2.3 in Schekochihin 2020). This 4/5 envelope can be interpreted as the strongest alignment sustainable in the tearing-mediated range, but it is not clear a priori what would emerge as a global feature in k space (i.e., resulting from a spatial average). The main difference between these two views depends on the details behind the X-point collapse (for a detailed discussion, see Section 7.4.1 in Schekochihin 2020). Although these two interpretations are not incompatible in term of the resulting fluctuations' spectrum, they could differ in terms of the effective scale-dependent alignment angle that can be *measured*.

We offer here a different point of view, somewhat *complementary* to the two summarized above. One can actually think about the ensemble of turbulent fluctuations as dynamically aligning (via the usual, non-tearing-mediated cascade) and misaligning (through tearing) in a patchy fashion in space and time, rather than stepwise in k space. This will likely result in a complicated convoluted state when globally averaged over the ensemble (i.e., not necessarily providing a clean, global $k_\perp^{4/5}$ scaling). Here, we illustrate this patchy-in-time behavior by distinguishing between those periods when the AW packets are shearing one another during their interaction ("overlap") and those periods during which the AW packets are instead far apart ("free cascade"). This will demonstrate that both states, a dynamically aligned cascade and a tearing-mediated misaligning cascade, are recursively realized in time. On the other hand, by performing the same time average as done for the fluctuations' spectra (which are indeed not affected by distinguishing between the above stages), we have found that $\sin\theta_\lambda$ exhibits ambiguous scalings (not shown). For our setup, *viz.*, AW-packet collisions, taking into account the patchiness in space appears to be less important (especially in the $\chi_0 \sim 0.1$ regime, where the largest-scale fluctuations affect much less the tearing-mediated regions). However, we expect that in simulations with broadband injection, this spatial patchiness should be carefully taken into account in order to capture the correct scalings of misalignment in the tearing-mediated range.

Analogously to the calculation of wavenumber anisotropy (Cho et al. 2002), we estimate the alignment angle θ between the velocity- and magnetic-field fluctuations at $k_\perp$ using[7]

$$\sin\theta_{k_\perp} = \frac{\left\langle \sum_{k\leqslant k_\perp<k+1} |\delta \boldsymbol{u}_{\perp,\lambda} \times \delta \boldsymbol{b}_{\perp,\lambda}| \right\rangle}{\left\langle \sum_{k\leqslant k_\perp<k+1} |\delta \boldsymbol{u}_{\perp,\lambda}||\delta \boldsymbol{b}_{\perp,\lambda}| \right\rangle}, \tag{4}$$

[7] In order to estimate $\sin\theta_{k_\perp}$ correctly, it is important to employ the averaging procedure $\langle|\delta \boldsymbol{u}_{\perp,\lambda} \times \delta \boldsymbol{b}_{\perp,\lambda}|\rangle/\langle|\delta \boldsymbol{u}_{\perp,\lambda}||\delta \boldsymbol{b}_{\perp,\lambda}|\rangle$ instead of a normalized version $\langle|\delta \boldsymbol{u}_{\perp,\lambda} \times \delta \boldsymbol{b}_{\perp,\lambda}|/(|\delta \boldsymbol{u}_{\perp,\lambda}||\delta \boldsymbol{b}_{\perp,\lambda}|)\rangle$. This is needed to select the "dynamically relevant" fluctuations, i.e., the averaging procedure should reflect the fact that, at a given scale λ, the fluctuations that contribute the most to the turbulent dynamics are those whose amplitudes are close to the rms value at that scale; see discussion in Mason et al. (2006).

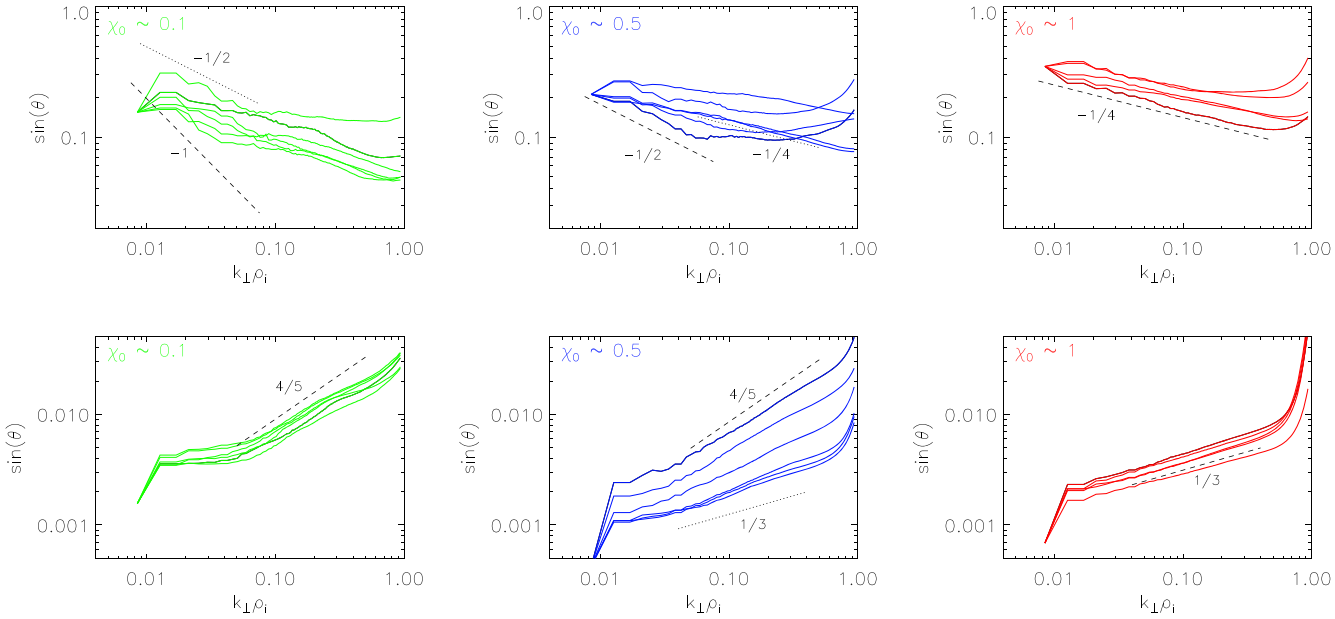

Figure 4. Variation of the alignment angle with scale for different initial values of the nonlinearity parameter χ_0 and at different times within developed turbulence ($0.9 \lesssim t/\tau_* \lesssim 1.7$): $\sin(\theta)$ vs. $k_\perp \rho_i$ at times when AW packets spatially overlap (top row) and when they are far apart (bottom row). Scale-dependent alignment is computed using Equation (4). Relevant power laws are provided for reference.

where the perpendicular direction is defined with respect to a scale-dependent mean field, $\langle \boldsymbol{B} \rangle_\lambda$, obtained by eliminating modes with $k_\perp > k/2 \sim 1/(2\lambda)$ from $\boldsymbol{B}$. Results for different simulations are shown in Figure 4, where we distinguish between the two main phases discussed above. During the interaction of the AW packets ("overlap"; top row), fluctuations get highly sheared and $\sin\theta_{k_\perp}$ clearly shows their tendency to align at decreasing scales. In the $\chi_0 \sim 1$ case, fluctuations align such that $\sin\theta_{k_\perp} \sim k_\perp^{-1/4}$, which matches the prediction by Boldyrev (2006). Note that, although this simulation seems to support the idea that dynamic alignment in strong turbulence is an effect that proceeds all the way down to dissipation scales (as observed by Perez et al. 2012), the limited resolution in our simulations cannot exclude the possibility that alignment is a finite-range effect that is tied to the dynamics at the outer scale and thus might stop before the dissipation scales are reached in the cascade (as claimed by Beresnyak 2012). The cases with smaller values of χ_0, on the other hand, exhibit stronger alignment: roughly as $k_\perp^{-1/2}$ for $\chi_0 \sim 0.5$ (perhaps reducing to $k_\perp^{-1/4}$ at the smallest scales, also showing small-scale flattening in some cases), and something in between $k_\perp^{-1}$ and $k_\perp^{-1/2}$ for $\chi_0 \sim 0.1$ (also exhibiting small-scale flattening in some cases). This behavior may be explained by the theory presented in Section 4.1. When AW packets are instead far apart ("free cascade"; bottom row), the fluctuations' dynamics is dominated by the tearing-mediated cascade and $\sin\theta_{k_\perp}$ exhibits a tendency to misalign. However, while the $\chi_0 \sim 0.1$ regime misaligns fluctuations roughly as $k_\perp^{4/5}$ for $k_\perp > k_*$ in all cases (as predicted by Boldyrev & Loureiro 2017), the intermediate $\chi_0 \sim 0.5$ case also shows times with a slightly weaker misalignment at $k_\perp > k_*$ in addition to the 4/5 scaling (somewhat between $k_\perp^{3/5}$ and $k_\perp^{1/2}$). This weaker dependence of the alignment angle at $\chi_0 \sim 0.5$ can be interpreted as the effect of some nonnegligible amount of the spatial patchiness discussed above, which is present in this regime despite our simple setup of AW-packet collisions (see Figure 2, middle row). During this "relaxation" stage, we also observe a weak misalignment for $\chi_0 \sim 1$, following approximately $k_\perp^{1/3}$ (without any obvious spectral breaks). We do not have any obvious explanation for this behavior at the moment, and further investigation would be required to address this point.

4. Dynamic Alignment and Reconnection in Weak Alfvénic Turbulence

Dynamic alignment of turbulent fluctuations is a necessary condition for the cascade to realize a tearing-mediated regime. To explain the evidence for this regime occurring in our simulations, we take a step back and postulate how dynamic alignment would affect the standard weak-turbulence phenomenology.

In this section, we provide a phenomenological description of weak turbulence in which dynamic alignment is occurring and discuss its implications for possible transitions to CB and/or tearing-mediated turbulence. For this purpose, we first establish our notation. Let us call λ the perpendicular length of fluctuations in the direction perpendicular to both the mean magnetic field at such scale, $\langle \boldsymbol{B} \rangle_\lambda$, and the perpendicular (to $\langle \boldsymbol{B} \rangle_\lambda$) magnetic-field fluctuations $\delta \boldsymbol{b}_{\perp,\lambda}$ (in Alfvénic units). Then, ℓ_λ and ξ_λ are the lengths of such fluctuations along $\langle \boldsymbol{B} \rangle_\lambda$ and along $\delta \boldsymbol{b}_{\perp,\lambda}$, respectively.[8] Quantities evaluated at the injection scale are adorned with a "0" subscript. Following Figure 3 of Boldyrev (2006), we define θ_λ as the angle between the flow- and magnetic-field fluctuations perpendicular to $\langle \boldsymbol{B} \rangle_\lambda$ at scale λ, $\delta \boldsymbol{u}_{\perp,\lambda}$ and $\delta \boldsymbol{b}_{\perp,\lambda}$, respectively. At the same time, if $\langle \boldsymbol{B} \rangle_\lambda$ differs from $\boldsymbol{B}_0$ by an angle $\tilde{\theta}_\lambda$, the angle between $\delta \boldsymbol{u}_\lambda$ and $\langle \boldsymbol{B} \rangle_\lambda$ is $\pi/2 - \tilde{\theta}_\lambda$. These two angles scale as $\theta_\lambda \sim \lambda/\xi_\lambda$ and $\tilde{\theta}_\lambda \sim \xi_\lambda/\ell_\lambda$, the total alignment angle between $\delta \boldsymbol{u}_\lambda$ and $\delta \boldsymbol{b}_\lambda$

[8] This distinction between the two scale-dependent transverse directions λ and ξ is ignored in Equation (4), consistent with the assumption that angular spectral averaging makes the difference between the variation scales transverse to the local field and the ambient field subdominant.

Table 1
Scalings Pertaining to Relevant Quantities and Critical Scales when Dynamic Alignment is Included in the Weak Turbulence Regime (Phenomenological Derivation; a "∼" Relating the Various Quantities to Their Scaling is Understood)

	Definition	Standard Weak Regime without Alignment ("W0")	Moderately Weak with Alignment ("WI")	Asymptotically Weak with Alignment ("WII")
$\tilde{\theta}_\lambda$	ξ_λ/ℓ_0	⋯	$(\lambda/\ell_0)^{1/2}$	const ($\ll\theta_\lambda$)
θ_λ	λ/ξ_λ	⋯	$(\lambda/\ell_0)^{1/2}$	(λ/ℓ_0)
eddies shape		elongated tubes ("spaghetti")	elongated ribbons ("fettuccine")	extended sheets ("lasagna")
$\tau_{\mathrm{nl},\lambda}/\tau_\mathrm{A}$	$\theta_\lambda^{-1}(\lambda/\ell_0)(v_\mathrm{A}/\delta b_\lambda)$	$\Lambda_0^{-1/4}(\lambda/\ell_0)^{1/2}$	$\Lambda_0^{-1/4}(\lambda/\ell_0)^{1/4}$	$\Lambda_0^{-1/4}=$ const
$\delta b_\lambda/v_\mathrm{A}$	$\Lambda_0^{1/4}\,\theta_\lambda^{-1/2}(\lambda/\ell_0)^{1/2}$	$\Lambda_0^{1/4}(\lambda/l_0)^{1/2}$	$\Lambda_0^{1/4}(\lambda/\ell_0)^{1/4}$	$\Lambda_0^{1/4}=$ const
$\mathcal{E}_{\delta b}/(l_0 v_\mathrm{A}^2)$	$\Lambda_0^{1/2}\,\theta_\lambda^{-1}(\lambda/\ell_0)^2$	$\Lambda_0^{1/2}(\lambda/l_0)^2$	$\Lambda_0^{1/2}(\lambda/\ell_0)^{3/2}$	$\Lambda_0^{1/2}(\lambda/\ell_0)$
$\lambda_\mathrm{CB}/\ell_0$	$\tau_{\mathrm{nl},\lambda_\mathrm{CB}}\sim\tau_\mathrm{A}$	$\Lambda_0^{1/2}$	Λ_0	⋯
λ_*/ℓ_0	$\gamma^\mathrm{t}_{\lambda_*}\,\tau_{\mathrm{nl},\lambda_*}\sim 1$	⋯	$\Lambda_0^{-1/9}S_0^{-4/9}$	$\Lambda_0^{-1/12}S_0^{-1/3}$

Notes. A "0" subscript denotes quantities evaluated at the injection scale, $\lambda\sim k_\perp^{-1}$ refers to the fluctuation's wavelength perpendicular to both a scale-dependent mean magnetic field $\langle\boldsymbol{B}\rangle_\lambda$ and to the fluctuations $\delta\boldsymbol{b}_\lambda$ themselves, $\tau_\mathrm{A}=\ell_0/v_\mathrm{A}$ is the Alfvén ("linear") time, and $v_\mathrm{A}=v_{\mathrm{A},0}=$ const is the Alfvén speed. We have introduced $\Lambda_0\doteq\varepsilon\ell_0/v_\mathrm{A}^3\sim\chi_0^2M_{\mathrm{A},0}^2$, where $\varepsilon\sim\varepsilon_0\sim u_0^2/\tau_0\sim\chi_0^2u_0^2/\tau_\mathrm{A}$ is the energy cascade (and injection) rate per unit mass, $\tau_0\sim\tau_{\mathrm{nl},0}^2/\tau_\mathrm{A}\sim\tau_\mathrm{A}/\chi_0^2$ is the cascade time at the outer scale, and $\chi_0=\tau_\mathrm{A}/\tau_{\mathrm{nl},0}$ and $M_{\mathrm{A},0}=u_0/v_\mathrm{A}$ are the nonlinearity parameter and Alfvénic Mach number at injection, respectively. Finally, $\gamma^\mathrm{t}_\lambda\,\tau_\mathrm{A}\sim S_0^{-1/2}(\lambda/\ell_0)^{-3/2}(\delta b_\lambda/v_\mathrm{A})^{1/2}$ is the maximal tearing growth rate (Loureiro & Boldyrev 2017; Mallet et al. 2017b), where $S_0\doteq\ell_0v_\mathrm{A}/\eta$ is the Lundquist number evaluated at the outer scale.

being $\phi_\lambda^\mathrm{ub}\simeq(\theta_\lambda^2+\tilde{\theta}_\lambda^2)^{1/2}$ (see Section 2 of Boldyrev 2006). In general, dynamic alignment weakens nonlinear interactions, $\mathcal{N}_\lambda\sim(\delta\boldsymbol{z}^+\cdot\boldsymbol{\nabla})\delta\boldsymbol{z}^-\sim(\delta\boldsymbol{z}^-\cdot\boldsymbol{\nabla})\delta\boldsymbol{z}^+\sim\phi_\lambda\delta z_\lambda^2/\lambda$, and simultaneously increases the cascade time $\tau_\lambda\sim\tau_{\mathrm{nl},\lambda}^2/\tau_\mathrm{A}\sim\tau_\mathrm{A}\phi_\lambda^{-2}(\lambda/\ell_0)^2(\delta z/v_\mathrm{A})^{-2}$, where now ϕ_λ is the angle between $\delta\boldsymbol{z}_\lambda^+$ and $\delta\boldsymbol{z}_\lambda^-$, $\tau_\mathrm{A}=\ell_0/v_\mathrm{A}$, and $v_\mathrm{A}=v_{\mathrm{A},0}=$ const.[9] (Note that, while we use the angle ϕ_λ (or, ϕ_λ^ub) in the phenomenological scaling, it is actually $\sin\phi_\lambda$ (or $\sin\phi_\lambda^\mathrm{ub}$) that enters the nonlinear term, so that its effect on nonlinearities is symmetric with respect to the fact that $\delta\boldsymbol{z}_\lambda^+$ and $\delta\boldsymbol{z}_\lambda^-$ (or, $\delta\boldsymbol{u}_\lambda$ and $\delta\boldsymbol{b}_\lambda$) can either align or counteralign.) In the following, we assume balanced turbulence at large scales,[10] $|\delta\boldsymbol{z}^+|^2\approx|\delta\boldsymbol{z}^-|^2$, so that ϕ_λ^ub scales as ϕ_λ, and we use the alignment angle θ_λ between $\delta\boldsymbol{u}_{\perp,\lambda}$ and $\delta\boldsymbol{b}_{\perp,\lambda}$ fluctuations as the relevant angle in the following phenomenological scalings. In fact, we will see that the scaling $\phi_\lambda^\mathrm{ub}\sim\theta_\lambda$ holds in all cases of interest. Moreover, θ_λ is the angle most relevant for the cascade of $\delta\boldsymbol{b}$ and $\delta\boldsymbol{u}$ fluctuations (this can be seen from the nonlinear terms, e.g., $(\delta\boldsymbol{u}\cdot\boldsymbol{\nabla})\delta\boldsymbol{b}$, in which the contribution from $\delta\boldsymbol{u}_{\parallel,\lambda}$ to $\delta\boldsymbol{u}\cdot\boldsymbol{\nabla}$, which is the one associated with the angle $\tilde{\theta}_\lambda$, is subdominant by a factor of $k_\parallel/k_\perp\ll1$).

4.1. Dynamic Alignment at Weak Nonlinearities

The fluctuations' scaling laws are derived by assuming a constant energy flux throughout each scale of the inertial range, viz. $\delta b_\lambda^2/\tau_\lambda\sim\varepsilon=$ const, and by adopting the weak-regime cascade time $\tau_\lambda\sim\tau_{\mathrm{nl},\lambda}^2/\tau_\mathrm{A}$. Taking into account alignment in $\tau_{\mathrm{nl},\lambda}\sim\lambda/(\theta_\lambda\delta b_\lambda)$, this leads to $\delta b_\lambda/v_\mathrm{A}\sim(\varepsilon\ell_0/v_\mathrm{A}^3)^{1/4}\,\theta_\lambda^{-1/2}(\lambda/\ell_0)^{1/2}$ and $\mathcal{E}_{\delta b}(\lambda)\propto(\varepsilon\ell_0/v_\mathrm{A}^3)^{1/2}\,\theta_\lambda^{-1}(\lambda/\ell_0)^2$. For convenience, the reader can find all of these definitions in the first column of Table 1.

When alignment is ignored, one obtains the usual weak-turbulence scalings (hereafter "W0") $\delta b_\lambda^{(\mathrm{W0})}\propto\lambda^{1/2}$ and $\mathcal{E}_{\delta b}^{(\mathrm{W0})}(\lambda)\propto\lambda^2$. This case does not include the fluctuations' anisotropy in the plane perpendicular to the mean magnetic field (i.e., turbulent eddies are very elongated "spaghetti"-like structures). It achieves CB at scale $\lambda_\mathrm{CB}^{(\mathrm{W0})}/\ell_0\sim(\varepsilon\ell_0/v_\mathrm{A}^3)^{1/2}\approx\chi_0M_{\mathrm{A},0}$, where $M_{\mathrm{A},0}\sim u_0/v_\mathrm{A}$ is the Alfvénic Mach number at injection (see second column of Table 1 for a summary of these scalings). Next we discuss how this picture might be modified by dynamic alignment. For the sake of clarity and simplicity, we consider here only two limiting cases that may be relevant for the interpretation of our simulation results; the general case will appear in a separate publication.

Using the maximal-alignment argument by Boldyrev (2006), in which $\tilde{\theta}_\lambda$ and θ_λ scale in the same way (as does ϕ_λ^ub), one obtains $\theta_\lambda\sim\tilde{\theta}_\lambda\propto\lambda^{1/2}$ (hereafter "WI"). This case develops 3D eddies with very elongated "fettuccine"-like structure (λ decreases faster than $\xi_\lambda\propto\lambda^{1/2}$, eventually attaining $\lambda\ll\xi_\lambda\ll\ell_0$). This regime is characterized by a spectrum $\propto k_\perp^{-3/2}$, as in Boldyrev (2006), but with $k_\parallel\sim$ const instead of $k_\parallel\propto k_\perp^{1/2}$. In this "WI" case, CB is reached at $\lambda_\mathrm{CB}^{(\mathrm{WI})}/\ell_0\sim\varepsilon\ell_0/v_\mathrm{A}^3\sim\chi_0^2\,M_{\mathrm{A},0}^2$, i.e., at scales typically smaller than those of "W0" due to weaker nonlinearities induced

[9] In general, it is not obvious whether one should define the alignment angle with respect to the fluctuations $\delta\boldsymbol{u}_\lambda$ and $\delta\boldsymbol{b}_\lambda$ or to the Elsässer fields $\delta\boldsymbol{z}_\lambda^+$ and $\delta\boldsymbol{z}_\lambda^-$. In fact, while both the original theory by Boldyrev (2006) and a number of in situ spacecraft measurements and of simulations' analyses focus on the former, showing the tendency of $\delta\boldsymbol{u}_\lambda$ and $\delta\boldsymbol{b}_\lambda$ to align with decreasing scales (e.g., Mason et al. 2006, 2011; Matthaeus et al. 2008; Podesta et al. 2009; Hnat et al. 2011; Perez et al. 2012), it should be the latter that directly enters the nonlinear term in the Elsässer formulation of the MHD equations (i.e., it is the $\delta\boldsymbol{z}^\pm$ that shear one another into alignment; see, e.g., Beresnyak & Lazarian 2006; Beresnyak 2012; Chandran et al. 2015; Mallet & Schekochihin 2017). Nevertheless, dynamic alignment of both $\delta\boldsymbol{u}_\lambda$ and $\delta\boldsymbol{b}_\lambda$ and of $\delta\boldsymbol{z}_\lambda^+$ and $\delta\boldsymbol{z}_\lambda^-$ are indeed simultaneously taking place (e.g., Wicks et al. 2013; Mallet et al. 2016). The angles between the two sets of fields are ultimately related by cross-helicity and residual energy, and both angles scale with λ in the same way under certain circumstances (see, e.g., Schekochihin 2020 for a more detailed discussion on this matter).

[10] Assuming balance at large scales does not imply that a scale-dependent imbalance and residual energy are not present, and actually, it can be seen from simple geometrical arguments that dynamic alignment indeed requires that both develop along the cascade.

by alignment. All of these scalings are conveniently summarized in the third column of Table 1. In this regard, we mention that a $\approx -3/2$ spectrum had been observed previously in high-resolution simulations of weak MHD turbulence by Meyrand et al. (2015); in these simulations, such a spectrum was found either as a large-scale range before transitioning into a smaller-scale standard weak-turbulence spectrum $\sim k_\perp^{-2}$, or as the fluctuations' spectrum when artificially removing $k_\parallel = 0$ modes (which indeed do not belong to the weak regime). The authors also report the emergence of strong intermittency, which they relate to the presence of intense current sheets (and perhaps one would recognize some plasmoid-like structures as well; see their Figure 1), in the plane perpendicular to $\boldsymbol{B}_0$. Although the realization of such a field-perpendicular anisotropy would indeed require some sort of dynamic alignment, the authors did not focus on this type of analysis, so at this stage we can only mention a plausible, qualitative connection with our predicted scalings.

Considering an asymptotically weak regime with $\delta b/B_0 \ll 1$ (hereafter "WII"), one can ignore the angle $\tilde{\theta}_\lambda$ between $\langle \boldsymbol{B} \rangle_\lambda$ and $\boldsymbol{B}_0$ with respect to θ_λ (hence, $\phi_\lambda^{\rm ub} \sim \theta_\lambda$). Since $\tilde{\theta}$ is finite for finite δb, we consider $\tilde{\theta}_\lambda \sim \xi_\lambda/\ell_0 \sim$ const $\ll \theta_\lambda$, so that $\xi_\lambda \sim$ const $\sim \xi_0$ and thus $\theta_\lambda \sim \lambda/\xi_\lambda \propto \lambda$. This case develops eddies that shrink only in the direction defined by λ, i.e., "lasagna"-like sheets (e.g., $\lambda \ll \xi_0 < \ell_0$ for very oblique AWs; this is reminiscent of our $\chi_0 \sim 0.1$ simulation). This regime is characterized by scale-invariant fluctuations $\delta b_\lambda \sim$ const, which thus produce a spectrum $\propto k_\perp^{-1}$, and by the fact that the cascade never reaches CB (because alignment depletes the nonlinearities so that $\tau_{{\rm nl},\lambda} \sim$ const). These scalings are repeated in the last column of Table 1. In this regard, it is worth mentioning that (rapid) scale-dependent alignment between $\delta \boldsymbol{u}_\perp$ and $\delta \boldsymbol{b}_\perp$ fluctuations (or antialignment between δz_λ^+ and δz_λ^-) has been reported to occur in the -1 spectral range of solar-wind turbulence by Wicks et al. (2013). This ensemble of aligning fluctuations was measured to constitute the majority of the fluctuations' population and to be the one responsible for the resulting -1 spectrum (structure functions show scale-independent behavior of $\delta b_\perp$ in that range; their Figure 1); they were interpreted as "nonturbulent" fluctuations, i.e., belonging to noninteracting (or weakly interacting) counterpropagating AWs. Despite the fact that here we do not take into account the effect of imbalance or residual energy, one may relate the fluctuations' behavior in Wicks et al. (2013) to the basic ideas underlying our "WII" case. In fact, in order to have dynamic alignment, such a population of counterpropagating AWs have to be shearing one another—and thus have a small, but finite, amount of nonlinear interactions (i.e., to be in the asymptotically weak $\chi \ll 1$ regime discussed above).

4.2. Dynamically Aligned, Weak Turbulence Meets Reconnection

Given the above scalings, cascading fluctuations should develop an anisotropy perpendicular to $\langle \boldsymbol{B} \rangle_\lambda$ that increases significantly faster than the one associated with a strong cascade ($\xi/\lambda \propto \lambda^{-1}$ for "WI" and $\propto \lambda^{-1/2}$ for "WII", instead of $\propto \lambda^{-1/4}$ in Boldyrev 2006). At the same time, turbulent eddies at a given scale live longer for weaker nonlinearities, leaving more time for tearing instability to grow. Thus, a transition to tearing-mediated turbulence should occur at larger scales when starting from a weakly nonlinear regime.

The critical scale λ_* at which tearing can grow on top of turbulent eddies is determined by requiring that the tearing growth timescale is comparable to the eddy lifetime, $\gamma_{\lambda_*}^{\rm t} \tau_{{\rm nl},\lambda_*} \sim 1$. Following Loureiro & Boldyrev (2017) and Mallet et al. (2017b), we adopt $\gamma_\lambda^{\rm t}\, \tau_{\rm A} \sim S_0^{-1/2} (\lambda/\ell_0)^{-3/2} (\delta b_\lambda/v_{\rm A})^{1/2}$ for the maximal tearing growth rate, where $S_0 \doteq \ell_0 v_{\rm A}/\eta$ is the Lundquist number evaluated at the outer scale. The transition scales in the "WI" and "WII" limits are summarized in Table 1.

The "WI" case can either transition to the "Boldyrev (2006)-type" of strong turbulence or to a tearing-mediated cascade: Since $\lambda_*^{\rm (WI)}/\lambda_{\rm CB}^{\rm (WI)} \sim \chi_0^{-20/9} M_{\rm A,0}^{-20/9} S_0^{-4/9}$, this means that tearing-mediated turbulence will prevail over the critically balanced cascade à la Boldyrev (2006) when $\chi_0 < M_{\rm A,0}^{-1} S_0^{-1/5}$. In this case, one requires only that $M_{\rm A,0} \sim 0.1$ and $S_0 \sim 10^5$ for the transition to the usual critically balanced cascade to be replaced by a transition to a tearing-mediated range for any $\chi_0 < 1$. On the other hand, tearing completely replaces the usual CB transition in case "WII". For instance, adopting a fixed Lundquist number S_0 across all regimes, one finds that $\lambda_*^{\rm (WI)}/\lambda_*^{\rm (CB)} \sim (\chi_0 M_{\rm A,0})^{-2/9} S_0^{8/63}$ and $\lambda_*^{\rm (WII)}/\lambda_*^{\rm (CB)} \sim (\chi_0 M_{\rm A,0})^{-1/6} S_0^{5/21}$, where $\lambda_*^{\rm (CB)}/\ell_0 \sim S_0^{-4/7}$ is the predicted transition scale in the strong, critically balanced regime (for $\chi_0 \sim 1$ and $M_{\rm A,0} \sim 1$) (Loureiro & Boldyrev 2017; Mallet et al. 2017b; Boldyrev & Loureiro 2017). More specifically, using the parameters of our $\chi_0 \sim 0.5$ simulation for case "WI", we predict a transition scale that is ≈ 6 times larger than the corresponding scale in the strong regime. Analogously, employing the parameters of the $\chi_0 \sim 0.1$ simulation for case "WII", we find a transition scale that would be ~ 60 times larger than the one predicted following a cascade à la Boldyrev (2006).

4.3. Conjecture of Tearing-driven CB

At this point, one may be tempted to derive the scalings for the tearing-mediated range in the weak regime by substituting $\tau_{{\rm nl},\lambda}$ with $\tau_\lambda^{\rm t} \sim 1/\gamma_\lambda^{\rm t}$ in the cascade time,[11] so that $\tau_\lambda \sim (\tau_\lambda^{\rm t})^2\, \tau_{\rm A}^{-1}$. However, a main feature of the weak regime, namely that $\ell_\lambda = \ell_0 =$ const, cannot hold if the cascade is mediated by tearing. This is because tearing will produce reconnecting magnetic islands and thereby generate smaller scales in the magnetic-field fluctuations, both in the perpendicular direction (λ and ξ_λ) and the parallel direction (ℓ_λ). How would ℓ_λ change, then? Since $\tau_\lambda^{\rm t}$ is now the timescale over which δb_λ fluctuations are generated at $\lambda < \lambda_*$, it is reasonable to consider that timescale to be the actual transfer time, viz., $\tau_\lambda \sim \tau_\lambda^{\rm t}$. Therefore, because of the condition $\tau_\lambda^{\rm t} \sim \tau_{{\rm nl},\lambda}$ and the fact that $\tau_\lambda \sim \tau_{{\rm nl},\lambda}^2/\tau_{\rm A}$ holds up to scale $\lambda \sim \lambda_*$, it follows that $\tau_\lambda^{\rm t} \sim \tau_{{\rm A},\lambda}$ (note that $\tau_{\rm A}$ is not scale-independent anymore below λ_*). This argument can explain the reduced number of AW-packet interactions required to achieve a fully developed turbulent state in our $\chi_0 \sim 0.5$ and $\chi_0 \sim 0.1$ simulations, viz., $N_{\rm int}^* \propto \chi_0^{-1}$ (Figure 1, left-panel inset). This indicates that, at scales $\lambda < \lambda_*$, CB should be expected to hold. We therefore conjecture that tearing drives the cascade toward CB and to the usual $-11/5$ spectrum of tearing-mediated turbulence.

5. Discussion and Conclusions

Using 3D gyrofluid simulations, we have investigated how the turbulent dynamics arising from collisions of

[11] Incidentally, this would lead to $\delta b_\lambda^{\rm (W,t)}/v_{\rm A} \sim (\varepsilon \ell_0/v_{\rm A}^3)^{1/3} S_0^{1/3} (\lambda/\ell_0)$, so that the spectrum would be $\mathcal{E}_{bb}^{\rm (W,t)} \propto \lambda^3 \sim k_\perp^{-3}$ and the alignment angle at $\lambda < \lambda_*$ would increase (i.e., fluctuations would misalign) as $\theta_\lambda^{\rm (W,t)} \propto \lambda^{-1} \sim k_\perp$.

counterpropagating AW packets with different large-scale nonlinearity parameter χ_0 is modified by tearing instability.

For strong initial nonlinearities ($\chi_0 \sim 1$), we observe a regime consistent with dynamically aligned, critically balanced MHD turbulence (Boldyrev 2006), i.e., fluctuations align accordingly to $\sin\theta_{k_\perp} \sim k_\perp^{-1/4}$, resulting in a $k_\perp^{-3/2}$ spectrum with $k_\parallel \propto k_\perp^{1/2}$ spectral anisotropy. Tearing does not appear to modify the cascade, consistent with theoretical expectations given the Lundquist numbers we are able to afford in our numerical simulations.

As the initial nonlinearities are lowered ($\chi_0 < 1$), however, a spectral break marking the transition between large-scale weak turbulence and small-scale tearing-mediated turbulence appears. The presence of a tearing-mediated range for small χ_0 implies that dynamic alignment occurs also at weak nonlinearities. In particular, for these cases the alignment angle shows a stronger scale dependence than found in the critically balanced regime, namely $\sin\theta_{k_\perp} \sim k_\perp^{-1/2}$ at $\chi_0 \sim 0.5$, and $\sin\theta_{k_\perp} \sim k_\perp^{-1}$ at $\chi_0 \sim 0.1$: This, combined with the increased lifetime of turbulent eddies at small χ_0, allows tearing to onset and mediate the cascade at scales larger than those predicted for a strong MHD cascade. Dynamic alignment in the weak regime also determines a modification to the large-scale spectrum, roughly scaling as $k_\perp^{-3/2}$ for $\chi_0 \sim 0.5$ and as $k_\perp^{-1}$ for $\chi_0 \sim 0.1$.

Regardless of the large-scale nonlinearity parameter, the emerging tearing-mediated range is consistent with the predicted $k_\perp^{-11/5}$ spectrum and a scale-dependent (mis)alignment of the fluctuations following something close to $\sin\theta_{k_\perp} \sim k_\perp^{4/5}$ (Mallet et al. 2017b; Boldyrev & Loureiro 2017; Comisso et al. 2018). These scalings, together with the fact that in our simulations the number of AW-packet interactions necessary to achieve a fully developed turbulent state for these low-χ_0 regimes is reduced with respect to the weak-turbulence expectation (viz. $\propto\chi_0^{-1}$ instead of $\propto\chi_0^{-2}$), support our conjecture of a "tearing-induced" transition to CB.

A phenomenological theory of dynamically aligned turbulence at weak nonlinearities that can explain these spectra and the transition to the tearing-mediated regime is provided. In particular, it is shown that, depending on the nonlinearity parameter at injection and on the large-scale Alfvénic-Mach and Lundquist numbers, the transition to tearing-mediated turbulence may compete with (if not completely supplant) the usual transition to CB; and that such a transition scale at small nonlinearities can be larger than the one implied by a critically balanced MHD cascade by several orders of magnitude, if the Lundquist number of the system is large enough (cf. Mallet et al. 2017b; Boldyrev & Loureiro 2017; Comisso et al. 2018). We expect such a shift of the transition scale λ_* to scales larger than those implied by a strong MHD cascade to be a general consequence of the fact that dynamic alignment occurs also in the weak regime, regardless of the precise physics of tearing (i.e., resistive or collisionless); the precise scaling of such a transition scale, on the other hand, will clearly depend upon the microphysics of tearing (e.g., Loureiro & Boldyrev 2017; Mallet et al. 2017a).

Our results suggest a more complex scenario than the simplistic picture of weak-to-strong transition in Alfvénic turbulence and shed new light on the existence of different large-scale regimes that coexist with tearing-mediated turbulence. This may have significant implications for small-scale dissipation and turbulent heating in space and astrophysical plasmas. Moreover, depending on the Lundquist number, a dynamically aligned weak cascade will undergo a transition to tearing-mediated turbulence at scales larger than the scales at which a standard weak cascade would meet the usual CB condition. Because this implies that a cascade in $k_\parallel$ is realized earlier in k (and with larger fluctuation amplitudes), our new scalings may have significant implications for the scattering efficiency of cosmic rays in astrophysical environments in which Alfvénic turbulence is injected with small nonlinearities and/or at small Alfvénic-Mach numbers (e.g., Chandran 2000; Yan & Lazarian 2002, 2008; Fornieri et al. 2021; Kempski & Quataert 2022).

Finally, our results and the basic ideas underlying our new scalings can be viewed in connection with in situ measurements of solar-wind turbulence. For instance, a (rapid) scale-dependent alignment between $\delta\boldsymbol{u}_\perp$ and $\delta\boldsymbol{b}_\perp$ fluctuations (or, antialignment between δz_λ^+ and δz_λ^-) has been reported to occur in the large-scale -1 range of solar-wind turbulence by Wicks et al. (2013). In particular, it was shown that such an ensemble of aligning fluctuations constitutes the majority of the fluctuations' population and that they are responsible for the resulting -1 spectrum (viz., structure functions reveal a scale-independent behavior of $\delta b_\perp$ in that range); these fluctuations were interpreted as "nonturbulent" fluctuations belonging to quasi-non-interacting, counterpropagating AWs. Since a finite, however small, amount of nonlinear interactions is required to occur for counterpropagating AWs to shear one another and induce dynamic alignment, we suggest that this may be the case for the aligning population observed by Wicks et al. (2013), thus potentially pertaining to an asymptotically weak ($\chi \ll 1$) regime as discussed in our scalings (Section 4.1, case "WII"). Another intriguing piece of in situ measurement is the one recently taken by Parker Solar Probe within the magnetically dominated corona (Kasper et al. 2021). Among other features, the magnetic-field spectrum in that region exhibits a transition between a $-3/2$ range and a steeper ≈ -2.2 slope occurring at scales (frequencies) much larger (smaller) than the ion characteristic scales (frequencies), which may be a hint of a potential large-scale, tearing-mediated range. While further studies are definitely needed to investigate the fluctuations' properties across this transition (e.g., estimated strength of nonlinearities, spectral anisotropy, etc.) in order to understand what type of transition we are observing, our theory in the moderately weak regime (Section 4.1, case "WI") provides an alternative scenario to interpret the measurements by Kasper et al. (2021).

While the underlying processes highlighted by the above in situ spacecraft measurements may be the same on which our scalings are founded (namely, dynamic alignment in the weak regime, followed by a large-scale transition to tearing-mediated turbulence), we caution as a final remark that these connections are purely conceptual, as our theory does not take into account imbalance or residual energy. With these being outside the scope of the current work, a more detailed theory that also includes these effects will be explored in a following paper.

The authors warmly acknowledge constructive advice from the anonymous referee, as well as productive comments by and discussions with Alexander Schekochihin following our posting of the original manuscript to arXiv. S.S.C. also acknowledges useful discussions with Alexandre Lazarian, after reporting the results presented in this manuscript at the 44th COSPAR Scientific Assembly in Athens, Greece. We gratefully acknowledge access to the Stellar cluster at the

PICSciE-OIT TIGRESS High Performance Computing Center and Visualization Laboratory at Princeton University, where the main simulations and analysis were performed. Computations were also performed on the "Mesocentre SIGAMM" machine, hosted by Observatoire de la Côte d'Azur. The authors warmly thank the organizers of the "Waves Côte d'Azur" conference in Nice (June 2019), where the first discussions leading to this work took place. M.W.K. thanks the Institut de Planétologie et d'Astrophysique de Grenoble (IPAG) for its hospitality and visitor support while this work was completed.

Appendix
Numerical Resolution, Lundquist Number, and Dissipation Operators

In this appendix, we summarize the outcome of various numerical tests that have been performed in preparation for the production runs. These tests focused on (i) the effectiveness of the numerical dissipation, (ii) the ability to identify clearly a tearing-mediated range, and (iii) the effect of employing different dissipation operators.

Point (i) has been addressed by increasing the resolution while fixing the large-scale properties and the dissipation parameters. The results of this convergence test are shown in the left panel of Figure 5, in which the time-averaged spectrum of $\delta B_\perp$ (and its local slope) versus $k_\perp \ell_0$ is reported for the $\chi_0 \sim 0.1$ regime and for two large-scale Lundquist number cases, $S \simeq 1.4 \times 10^6$ (yellow dashed and black dotted lines) and $S \simeq 1.7 \times 10^6$ (green solid and black dashed lines) at different small-scale resolutions. The overlap of the spectra and of their local slopes at increased resolution shows the effectiveness of the dissipation parameters employed (hereafter referred to as "optimal").

Point (ii) has been addressed by keeping the small-scale resolution and (optimal) dissipation parameters fixed, while the Lundquist number $S = L_0 v_A/\eta$ has been varied by changing the injection scale L_0. A summary of this study is reported in the left panel of Figure 5, in which spectra of $\delta B_\perp$ (and their local slopes) versus $k_\perp \ell_0$ are shown for different Lundquist numbers at $\chi_0 \sim 0.5$ (upper spectra, in blue shades and different line styles) and at $\chi_0 \sim 0.1$ (lower spectra, green/yellow/orange/black colors and different line styles). Although the existence of a $-11/5$ range seems to be visible already at the lowest Lundquist numbers, a reliable and fairly extended tearing-mediated spectrum is obviously achieved only at the largest separation of scales (i.e., larger L_0 at fixed dissipation scales, corresponding to larger S). In this context, the values $S \simeq 1.7 \times 10^6$ and $S \simeq 3.3 \times 10^5$ for the $\chi_0 \sim 0.1$ and $\chi_0 \sim 0.5$ regimes, respectively, were considered to provide a satisfactory result.

Finally, the impact of the dissipation order has been explored by varying the operators employed and/or by taking a combination of different orders. The outcome is summarized in the right panel of Figure 5, which shows spectra of $\delta B_\perp$ and their local slopes versus $k_\perp \rho_i$ in the $\chi_0 \sim 0.5$ regime when using (a) only a Laplacian operator ($\propto k^2$, orange dashed line; note that to obtain a $-11/5$ range for this case, the dissipation level is insufficient and thus energy accumulates at the smallest scales of the system–and so the simulation is considered to be "unresolved"), (b) only an eighth-order operator ($\propto k^8$, light-blue dashed–three-dotted line), or (c) a combination of Laplacian and eighth-order operators (blue solid line; this simulation corresponds to the purple dashed line in the left panel of Figure 5, i.e., $S \simeq 2.8 \times 10^5$ on a 560^3 grid). Although the fluctuations' spectrum for the case with only Laplacian dissipation clearly shows a slight rise of the spectral slope at $k_\perp \rho_i > 0.2$, it overlaps in the range $k_\perp \rho_i \lesssim 0.2$ with the spectrum obtained from the (well-resolved) simulation employing both Laplacian and eighth-order dissipation operators. We are therefore confident that, in the latter case, the break scale $k_\perp^* \rho_i \approx 0.07$ and the $-11/5$ slope in the range $0.08 \lesssim k_\perp \rho_i \lesssim 0.2$ are due to the usual resistive reconnection (while the additional hyperresistivity simply completes the energy dissipation at the smallest scales of the system). On the other hand, there is no clear signature of a tearing-mediated $-11/5$ range in the spectrum obtained from the simulation employing only an eighth-order dissipation operator; although an apparent break at $k_\perp \rho_i \sim 0.06$ followed by a ≈ -1.85 slope in the range $0.07 \lesssim k_\perp \rho_i \lesssim 0.15$ seems to be present, this may be due to other effects rather than (hyperresistive) reconnection (which would instead exhibit a $-19/7 \approx -2.7$ slope, according to predictions by Boldyrev & Loureiro 2017). The reason for this slope in the purely hyperresistive case is not clear at this stage and will require further investigation.

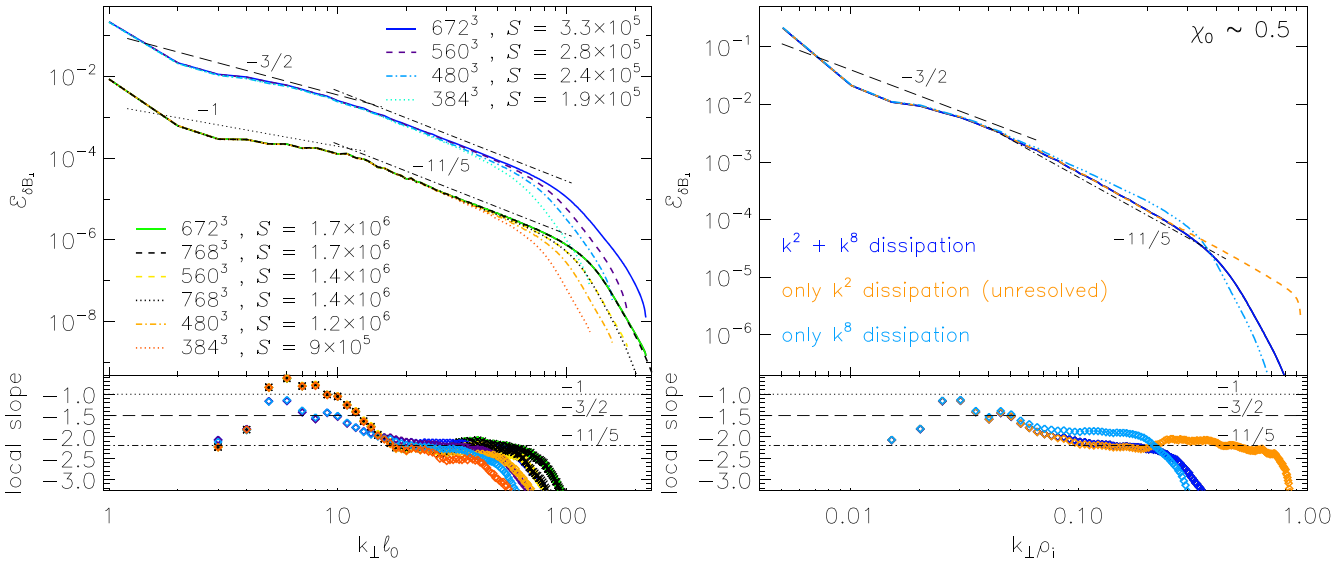

Figure 5. Left: time-averaged energy spectrum of $\delta B_\perp$ fluctuations and its local slope vs. $k_\perp \ell_0$ for different Lundquist numbers and/or resolutions, at $\chi_0 \sim 0.5$ (upper spectra, in blue shades and different line styles) and at $\chi_0 \sim 0.1$ (lower spectra, green/yellow/orange/black colors and different line styles). The Lundquist number $S = L_0 v_A/\eta$ has been varied by changing L_0 at fixed resolution. Two examples of different resolutions at fixed $\chi_0 \sim 0.1$ exhibit the same behavior ($L_0 \simeq 1244\rho_i$ and $S \simeq 1.4 \times 10^6$, yellow dashed and black dotted lines; $L_0 \simeq 1493\rho_i$ and $S \simeq 1.7 \times 10^6$, green solid and black dashed lines), demonstrating numerical convergence for the chosen dissipation parameters. Right: time-averaged $\delta B_\perp$ spectrum and its local slope vs. $k_\perp \rho_i$ at $\chi_0 \sim 0.5$ for different combinations of dissipation operators, viz., only Laplacian dissipation ($\propto k^2$, orange dashed line), only eighth-order dissipation ($\propto k^8$, light-blue dashed–three-dotted line), and a combination of both Laplacian and eighth-order dissipation (blue solid line; this corresponds to the purple dashed line in the left panel, i.e., $S \simeq 2.8 \times 10^5$). This shows that, when a combination of the two operators is employed, our choice of dissipation parameters is such that the tearing-mediated range $\propto k_\perp^{-11/5}$ is due to the usual (i.e., Laplacian) resistivity.

ORCID iDs

S. S. Cerri https://orcid.org/0000-0003-0562-6574
T. Passot https://orcid.org/0000-0002-6845-9729
D. Laveder https://orcid.org/0000-0003-0331-6206
P.-L. Sulem https://orcid.org/0000-0002-6231-5126
M. W. Kunz https://orcid.org/0000-0003-1676-6126

References

Agudelo Rueda, J. A., Verscharen, D., Wicks, R. T., et al. 2021, JPlPh, 87, 905870228
Alexandrova, O., Jagarlamudi, V. K., Hellinger, P., et al. 2021, PhRvE, 103, 063202
Alexandrova, O., Saur, J., Lacombe, C., et al. 2009, PhRvL, 103, 165003
Arzamasskiy, L., Kunz, M. W., Chandran, B. D. G., & Quataert, E. 2019, ApJ, 879, 53
Beresnyak, A. 2012, MNRAS, 422, 3495
Beresnyak, A., & Lazarian, A. 2006, ApJL, 640, L175
Biskamp, D., & Müller, W.-C. 2000, PhPl, 7, 4889
Boldyrev, S. 2006, PhRvL, 96, 115002
Boldyrev, S., & Loureiro, N. F. 2017, ApJ, 844, 125
Bruno, R., & Carbone, V. 2013, LRSP, 10, 2
Carbone, V., Veltri, P., & Mangeney, A. 1990, PhFlA, 2, 1487
Cerri, S. S., Arzamasskiy, L., & Kunz, M. W. 2021, ApJ, 916, 120
Cerri, S. S., & Califano, F. 2017, NJPh, 19, 025007
Cerri, S. S., Grošelj, D., & Franci, L. 2019, FrASS, 6, 64
Cerri, S. S., Kunz, M. W., & Califano, F. 2018, ApJL, 856, L13
Cerri, S. S., Servidio, S., & Califano, F. 2017, ApJL, 846, L18
Chandran, B. D. G. 2000, PhRvL, 85, 4656
Chandran, B. D. G., Schekochihin, A. A., & Mallet, A. 2015, ApJ, 807, 39
Chen, C. H. K. 2016, JPlPh, 82, 535820602
Chen, C. H. K., Bale, S. D., Bonnell, J. W., et al. 2020, ApJS, 246, 53
Cho, J., Lazarian, A., & Vishniac, E. T. 2002, ApJL, 566, L49
Comisso, L., Huang, Y.-M., Lingam, M., Hirvijoki, E., & Bhattacharjee, A. 2018, ApJ, 854, 103
Coppi, B., Galvao, R., Pellat, R., Rosenbluth, M., & Rutherford, P. 1976, FizPl, 2, 961
Dong, C., Wang, L., Huang, Y.-M., Comisso, L., & Bhattacharjee, A. 2018, PhRvL, 121, 165101
Elsässer, W. M. 1950, PhRv, 79, 183
Fornieri, O., Gaggero, D., Cerri, S. S., De La Torre Luque, P., & Gabici, S. 2021, MNRAS, 502, 5821
Franci, L., Cerri, S. S., Califano, F., et al. 2017, ApJL, 850, L16
Goldreich, P., & Sridhar, S. 1995, ApJ, 438, 763
Goldstein, M. L., Roberts, D. A., & Matthaeus, W. H. 1995, ARA&A, 33, 283
González, C. A., Parashar, T. N., Gomez, D., Matthaeus, W. H., & Dmitruk, P. 2019, PhPl, 26, 012306
Grošelj, D., Cerri, S. S., Bañón Navarro, A., et al. 2017, ApJ, 847, 28
Hnat, B., Chapman, S. C., Gogoberidze, G., & Wicks, R. T. 2011, PhRvE, 84, 065401
Howes, G. G., & Nielson, K. D. 2013, PhPl, 20, 072302
Howes, G. G., Tenbarge, J. M., Dorland, W., et al. 2011, PhRvL, 107, 035004
Huang, Y.-M., & Bhattacharjee, A. 2016, ApJ, 818, 20
Iroshnikov, P. S. 1963, AZh, 40, 742
Kasper, J. C., Klein, K. G., Lichko, E., et al. 2021, PhRvL, 127, 255101
Kempski, P., & Quataert, E. 2022, MNRAS, 514, 657
Kraichnan, R. H. 1965, PhFl, 8, 1385
Loureiro, N. F., & Boldyrev, S. 2017, PhRvL, 118, 245101
Loureiro, N. L., & Boldyrev, S. 2017, ApJ, 850, 182
Mallet, A., & Schekochihin, A. A. 2017, MNRAS, 466, 3918
Mallet, A., Schekochihin, A. A., Chandran, B. D. G., et al. 2016, MNRAS, 459, 2130
Mallet, A., Schekochihin, A. A., & Chandran, B. D. G. 2017a, JPlPh, 83, 905830609
Mallet, A., Schekochihin, A. A., & Chandran, B. D. G. 2017b, MNRAS, 468, 4862
Mason, J., Cattaneo, F., & Boldyrev, S. 2006, PhRvL, 97, 255002
Mason, J., Perez, J. C., Cattaneo, F., & Boldyrev, S. 2011, ApJL, 735, L26
Matthaeus, W. H., Parashar, T. N., Wan, M., & Wu, P. 2016, ApJL, 827, L7
Matthaeus, W. H., Pouquet, A., Mininni, P. D., Dmitruk, P., & Breech, B. 2008, PhRvL, 100, 085003
Meyrand, R., Kiyani, K. H., & Galtier, S. 2015, JFM, 770, R1
Miloshevich, G., Laveder, D., Passot, T., & Sulem, P. L. 2021, JPlPh, 87, 905870201
Oughton, S., & Matthaeus, W. H. 2020, ApJ, 897, 37
Passot, T., & Sulem, P. L. 2019, JPlPh, 85, 905850301
Passot, T., Sulem, P. L., & Laveder, D. 2022, JPlPh, 88, 905880312
Passot, T., Sulem, P. L., & Tassi, E. 2018, PhPl, 25, 042107
Perez, J. C., Mason, J., Boldyrev, S., & Cattaneo, F. 2012, PhRvX, 2, 041005
Perrone, D., Passot, T., Laveder, D., et al. 2018, PhPl, 25, 052302
Pezzi, O., Parashar, T. N., Servidio, S., et al. 2017, JPlPh, 83, 705830108
Podesta, J. J., Chandran, B. D. G., Bhattacharjee, A., Roberts, D. A., & Goldstein, M. L. 2009, JGRA, 114, A01107

Politano, H., Pouquet, A., & Sulem, P. L. 1995, PhPl, 2, 2931
Quataert, E., & Gruzinov, A. 1999, ApJ, 520, 248
Ripperda, B., Mahlmann, J. F., Chernoglazov, A., et al. 2021, JPlPh, 87, 905870512
Sahraoui, F., Goldstein, M. L., Belmont, G., Canu, P., & Rezeau, L. 2010, PhRvL, 105, 131101
Sahraoui, F., Hadid, L., & Huang, S. 2020, RvMPP, 4, 4
Schekochihin, A. A. 2020, arXiv:2010.00699
Schekochihin, A. A., & Cowley, S. C. 2006, PhPl, 13, 056501
Servidio, S., Dmitruk, P., Greco, A., et al. 2011, NPGeo, 18, 675
Sisti, M., Fadanelli, S., Cerri, S. S., et al. 2021, A&A, 655, A107
Squire, J., Meyrand, R., Kunz, M. W., et al. 2022, NatAs, 6, 715
Tenerani, A., & Velli, M. 2020, MNRAS, 491, 4267
Told, D., Jenko, F., TenBarge, J. M., Howes, G. G., & Hammett, G. W. 2015, PhRvL, 115, 025003
Verniero, J. L., Howes, G. G., & Klein, K. G. 2018, JPlPh, 84, 905840103
Wan, M., Oughton, S., Servidio, S., & Matthaeus, W. H. 2012, JFM, 697, 296
Wicks, R. T., Horbury, T. S., Chen, C. H. K., & Schekochihin, A. A. 2010, MNRAS, 407, L31
Wicks, R. T., Mallet, A., Horbury, T. S., et al. 2013, PhRvL, 110, 025003
Yan, H., & Lazarian, A. 2002, PhRvL, 89, 281102
Yan, H., & Lazarian, A. 2008, ApJ, 673, 942
Zhdankin, V., Uzdensky, D. A., & Boldyrev, S. 2015, ApJ, 811, 6
Zhdankin, V., Uzdensky, D. A., Perez, J. C., & Boldyrev, S. 2013, ApJ, 771, 124